Article

Performance Evaluation of a Novel Propulsion System for the Spherical Underwater Robot (SURIII)

Shuoxin Gu [1] (ID) **and Shuxiang Guo [2,3,*]**

[1] Graduate School of Engineering, Kagawa University, Takamatsu, Kagawa 760-0396, Japan; s16d642@stu.kagawa-u.ac.jp
[2] Key Laboratory of Convergence Medical Engineering System and Healthcare Technology, The Ministry of Industry and Information Technology, School of Life Science, Beijing Institute of Technology, Beijing 100081, China
[3] Department of Intelligent Mechanical Systems Engineering, Kagawa University, Takamatsu, Kagawa 760-0396, Japan
* Correspondence: guo@eng.kagawa-u.ac.jp

Abstract: This paper considers a novel propulsion system for the third-generation Spherical Underwater Robot (SURIII), the improved propulsion system is designed and analyzed to verify its increased stability compared to the second-generation Spherical Underwater Robot (SURII). With the new propulsion system, the robot is not only symmetric on the X axis but also on the Y axis, which increases the flexibility of its movement. The new arrangement also reduces the space constraints of servomotors and vectored water-jet thrusters. This paper also aims to the hydrodynamic characteristic of the whole robot. According to the different situations of the surge and heave motion, two kinds of methods are used to calculate the drag coefficient for the SURIII. For surge motion, the drag coefficient can be determined by the Reynolds number. For heave motion, considering about the influences of edges and gaps of the SURIII, the drag coefficient needs to be calculated by the dynamic equation. In addition, the Computational Fluid Dynamics (CFD) simulation is carried out to estimate some parameters which cannot be measured. The pressure contours, velocity vectors and velocity streamlines for different motions are extracted from the post-processor in the CFD simulation. The drag coefficients of surge and heave motion are both calculated by the simulation results and compared with the chosen one by Reynolds number. Finally, an experiment is also conducted for measure the propulsive force of the multi-vectored water-jet thrusters by using a 6-DoF load cell. The experimental results demonstrate the propulsive force is better than a previous version. Thus, the propulsive performance is better than before.

Keywords: spherical underwater robot; hydrodynamic analysis; Computational Fluid Dynamics simulation; propulsion system; vectored water-jet thrusters

1. Introduction

With the unceasing underwater exploration of the ocean, autonomous underwater vehicles (AUVs) have also been improved and developed for underwater detection. If AUVs in the unknown underwater environment can still maintain adequate flexibility and sensitivity, they can be suitable for a variety of complex underwater tasks. The IFREMER L'Eqaulard AUV was probably the first AUV which deployed for marine geoscience [1,2]. Anirban Mazumdar et al. developed a ball shaped underwater robot which was completely smooth and used jets to propel and maneuver through water-filled environments such as the inside of nuclear power plants [3]. MIT researchers also unveiled an oval-shaped submersible robot smaller than a football, flattened on one side and able to slide along an underwater surface to perform ultrasound scans [4]. But these two kinds of robots are both designed

for special environments such as pipelines or confined spaces, with relatively simple forward and backward motion. Heejoong Kim and Jihong Lee proposed a swimming pattern generator mimicking locomotion of diving beetles with the viewpoint of biomimetics for legged underwater robots [5]. In our previous study, firstly a spherical underwater robot with multi vectored water-jet thrusters was developed [6,7]. Then a Father-son Underwater Intervention Robotic System (FUIRS) was proposed [8]. In this system, the SURII plays the role of the father robot and the micro robot plays the role of the son robot [9]. The father robot has a spherical shape and a vectored water-jet-based propulsion system, so it can work with high stability and low noise. The FUIRS system is shown in Figure 1. With the development of the previous research, the SURIII which has four vectored water-jet thrusters for the propulsion system is proposed [10–12].
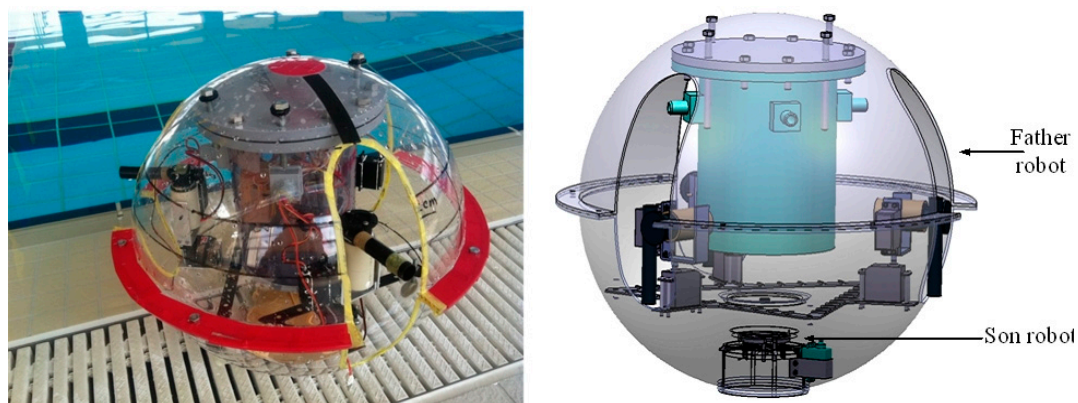

Figure 1. Father-son Underwater Intervention Robot System (FUIRS).

AUVs face different working conditions, requiring different configurations and size, thus many new underwater technologies are being explored and applied to AUVs. Because of the excellent diving capability of underwater creatures, some underwater robots are designed to mimic their characteristics. Hyung-Jung Kim et al. developed a turtle-like swimming robot with biomimetic flippers. This robot uses a smart soft composite structure to realize smooth and soft flapping motion [13]. Guo lab in Kagawa University developed an octopus-inspired micro robot using ionic polymer metal composite (IPMC). It can cooperate with other robot to execute underwater intervention tasks [14]. These above robots imitate the appearance or movement of aquatic creatures to better adapt to the underwater environment. Watson S. A. et al. developed a micro-spherical underwater robot which used six propellers to generate propulsive force and this robot was designed for monitoring the nuclear storage pond and preventing leakage in wastewater treatment facilities [15,16]. However, its propeller thruster cannot adjust direction. MIT researchers designed a robot called "Omni-Egg", which is smooth, spheroidal and completely appendage-free [17]. It used a novel pump-jet system built into the streamlined shell. Researchers at Harbin Engineering University also developed a spherical underwater robot with three water-jet thrusters [18,19].

Spherical Underwater Robot (SUR) is a kind of special structural underwater robot which has better compression performance. Due to its overall symmetry, there are no coupling items in fluid dynamics calculation and the hydrodynamic parameters are also equal. Therefore, it has more extensive application. In this paper, a novel spherical underwater robot (SURIII) which has four vectored water-jet thrusters was developed. A novel annular symmetrical structure was proposed to ensure the stability of the propulsion system. The static analysis proved that this new structure is more stable than before. The improvement of structure increases the utilization of space. Therefore, the rotation angle of vectored water-jet thrusters is more varied and flexible. Hydrodynamic characteristics are the key point and difficulty for underwater robot research. In CFD simulation, the pressure contours, velocity vectors and velocity streamlines are obtained from the post-processor.

This paper is organized as follows. Section 2 presents the mechanical design and analysis of the SURIII. Analysis of the hydromechanics of the vehicle, including hydrodynamic analysis of the impact of propulsion system deformation on vehicle stability as well as calculation of drag characteristics, are presented in Section 3. The results of the CFD simulation carried out by ANSYS-CFX are presented in Section 4. Experimental evaluation of the propulsive force of the propulsion system is described in Section 5. Finally, some conclusions are provided in Section 6.

2. Mechanical Design and Analysis

2.1. Inspiration for Design

The inspiration for the design of the SUR propulsion system came from the propulsive mechanism of the jellyfish. A study indicated that jellyfish are the most energy efficient underwater swimmers [20]. Figure 2 demonstrates how jellyfish, through the alternate contraction and relaxation of their bodies, produce a jet of water whose propulsive force propels them through the water. The design of the vehicle, as described subsequently, is aimed at mimicking the efficient motion of the jellyfish and attaining symmetry, stability and performance.
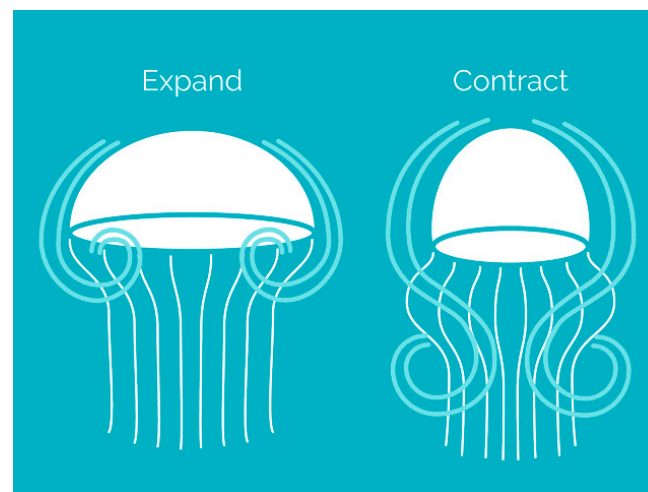

Figure 2. Propulsion mechanism of the Jellyfish.

2.2. Mechanical Design and Analysis of Propulsion System

Taking the requirement of volume into consideration, SUR as a kind of small underwater robot in our lab, its movement is restricted by the structure and space. Thus, its propulsion system needs to be improved in the limited space to enhance the hydrodynamic property. In the propulsion system of the SURII, three water-jet thrusters were homogeneously located on an equilateral triangle support as shown in Figure 3. This kind of layout limited the rotation angle of servo motors, thereby effecting the movement performance, especially the forward movement. Such a structure cannot achieve the maximum propulsive force and the payload capability will be affected. In terms of the current issue, a novel annular symmetrical mechanism is designed for the propulsion system of SURIII as illustrated in Figure 4. This system adopts an annular structure which can provide support for four thrusters. The maximum distance between the two opposite thrusters is 48 cm, the inside diameter of the annular support is 19 cm and its thickness is 0.5 cm. Considering the size of spherical hull, the weight of the robot and advantages of symmetric structure, only one more set thruster is added. Moreover, the stability of robot will be impacted less while improving the dynamic power. In order to enhance the stiffness of the propulsion system, the annular support structure is fixed with the waterproof bin by jackscrews.
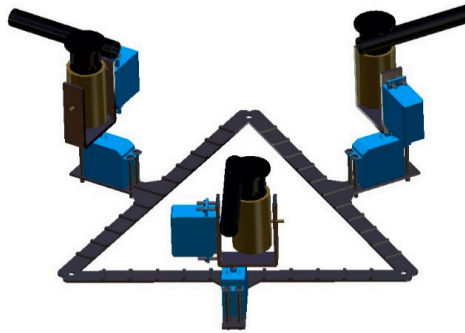
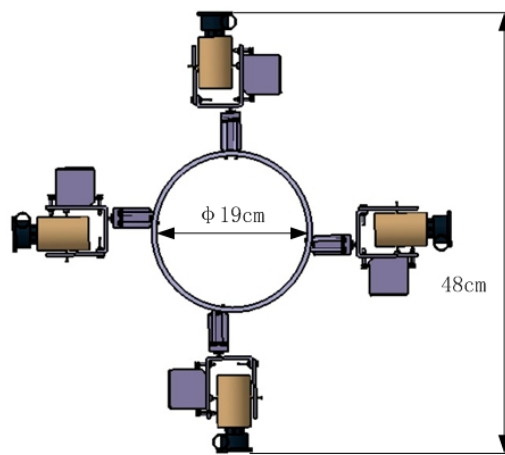**Figure 3.** Propulsion system of SURII.

Figure 4. Propulsion system of SURIII.

For the novel propulsion system, the static analysis is necessary to evaluate its performance. Above all, unforeseen deformation will adversely affect the robot, particularly the direction of the nozzle. Although the second-generation robot has already enhanced the rotation support between servo motors and the water-jet thruster and reduced the deformation of the system [21], its triangle support is only suitable for three water-jet thrusters and cannot be used for fours. Therefore, the deformation analysis for the annular support is very important. Moreover, the weight of the propulsion system is increased after adding one more set of vectored water-jet thruster, hence the static analysis is quite essential.

The basic movements of the robot include three motions: up, down and forward motion. Based on this, the static analysis is carried out by the ANSYS WORKBENCH. Figure 5 illustrates the simulation models of the different motions for SURIII. The up and down motion models are shown in Figure 5a,c, the 2 N force is applied to each nozzle, respectively. The forward motion model is shown in Figure 5b, the 2 N force is exerted on three working nozzles. The position and direction of these forces are the same as the static analysis of the SURII. Both the triangle support of the SURII and the annular support of the SURIII are fixed with the ground.

Figure 6 displays the deformation of the propulsion system. Figure 6a,b describe the deformation of the previous and the novel propulsion system, respectively. According to the rainbow map in the left of the interface, red color indicates the maximum deformation in the result. Observing these two propulsion systems, the maximum deformation occurs at the same location, therefore the maximum deformation of these two propulsion systems is compared to evaluate the stiffness. Figure 7 is the comparison of the maximum deformation between these two propulsion systems. From the comparison, it is evident that no matter what kind of motion state, the deformation of propulsion system in SURIII is smaller than that in SURII. However, the maximum deformation (0.045 mm) of all

motions for SURIII which generates in the up motion is still far less than the minimum deformation (0.422 mm) of all motions for SURII which generates in the down motion.
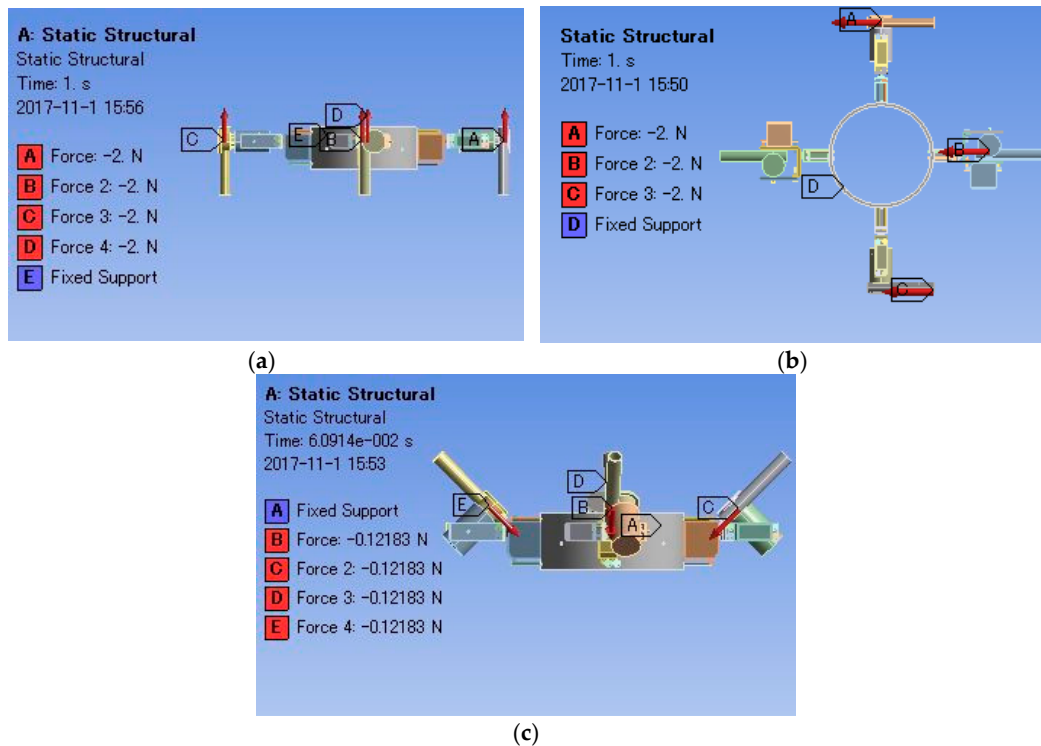

(**a**)
(**b**)

(**c**)

Figure 5. The pre-process of the static analysis. (**a**) Up motion; (**b**) Forward motion; (**c**) Down motion.
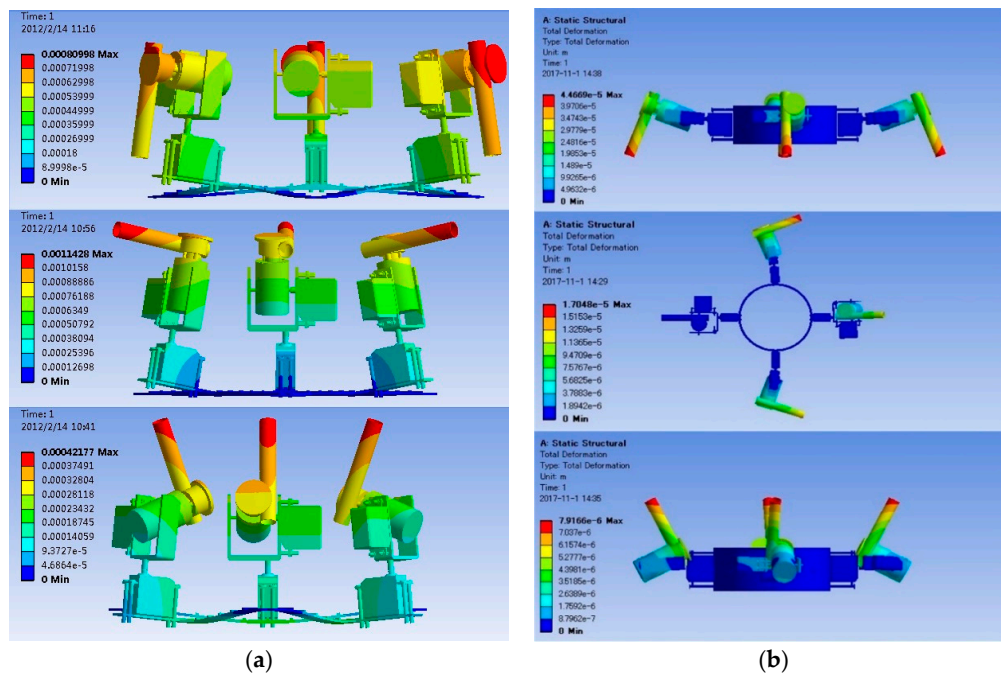

(**a**)
(**b**)

Figure 6. Deformation of the propulsion system. (**a**) Deformation of the propulsion system for SURII; (**b**) Deformation of the propulsion system for SURIII.
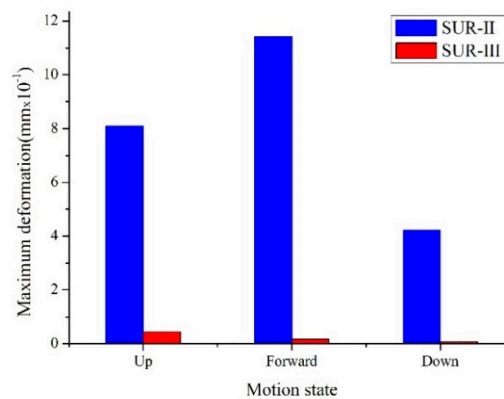
Figure 7. Deformation comparison of SURII and SURIII.

Due to the good characteristics of the vectored water-jet thruster, this part uses the previous design. Each set of vectored water-jet thruster is composed of four parts, which includes a water-jet thruster, a waterproof box for protecting DC motor, two servo motors and a support for them. The propulsive force of the SURIII comes from vectored water-jet thrusters and the orientation of propulsive force can be controlled by the rotation angle of two servo motors.

Two servo motors are rotated in two planes which are vertically intersecting, so they provide two rotational DoFs for the thruster. Figure 8 shows the rotation range of these two servo motors. From the side view of vertical motion in Figure 8a, the nozzle turns 45° counter clockwise, the robot will move down underwater. When the nozzle turns 90° clockwise, the robot will move up to the surface of water. And from the top view of forward motion in Figure 8b, the robot will move forward when the nozzle turns 90° clockwise. If servo motor 1 rotates 180° in the forward motion and then the nozzle turns 90° counter clockwise as shown in Figure 8c, the robot will change from forward motion to backward motion quickly without any change in heading. In other words, through the simultaneous action of these two servo motors, the water-jet thruster can rotate from −90° to 90° in horizontal plane. This angle will affect the orientation of horizontal motions and the orientation can be changed directly by rotating two servo motors. Besides the down motion, all the other motions have the same orientations with the propulsive force and this can maximize the use of it.
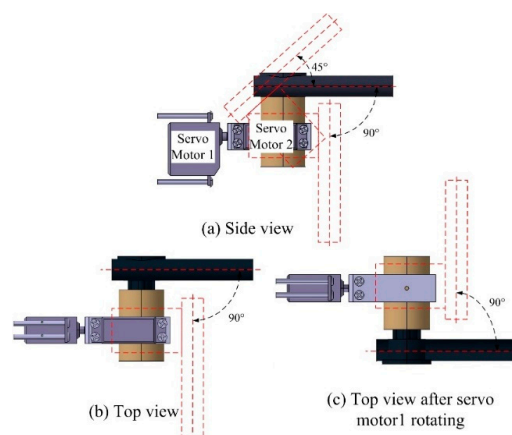

Figure 8. The nozzle angle of different motion states.

2.3. Structure Design of SURIII

In SURIII the design of the propulsion system is improved. The fixed form of the waterproof bin and design of the spherical hull should be changed to fit the new structure. The 3D model of the

SURIII is illustrated in Figure 9. All control circuits are collected in the waterproof bin. Four screws are used to hold up the waterproof bin in the hull. For the spherical hull, it needs to be made four symmetrical openings for four vectored water-jet thrusters. In order to prevent interference between the spherical hull and thrusters and ensure the stiffness of the hull, the opening is designed as shown in Figure 9. The middle part opens wide and both ends open narrowly. Furthermore, on the one hand the hull can block the external damage to protect the internal structure, on the other hand the spherical hull can realize a zero turning radius smoothly.
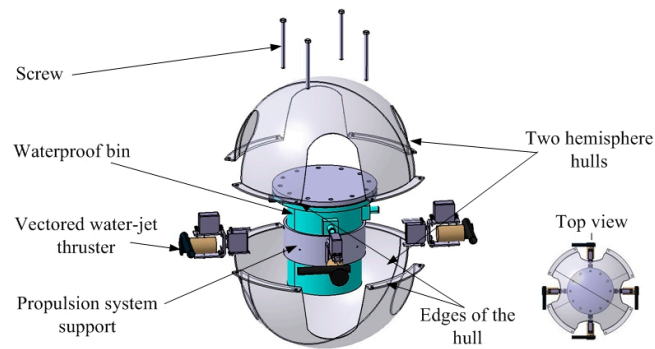

Figure 9. 3D model of SURIII.

2.4. Motions of SURIII

Degrees of freedom (DoF) for the underwater robot include surge, sway, heave, roll, pitch and yaw. Table 1 summarizes the utilization ratios of different degrees of freedom for an underwater robot. DoFs as sway, roll and pitch are rarely used [22].

In SURIII, there are four DoF which involve surge, sway, heave and yaw. These DoFs are shown in Figure 10. There are four water-jet thrusters in the robot and the inclined angle between two thrusters is 90 degrees, so it can be switched between the surge and sway directly by changing the working thrusters.

Table 1. Utilization ratio of different DoFs.

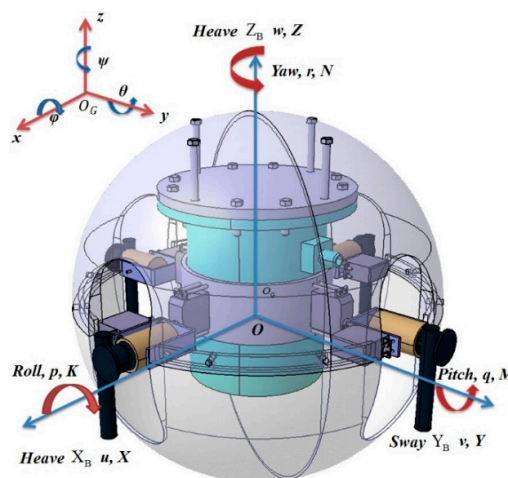| DoF	Surge	Sway	Heave	Roll	Pitch	Yaw
Utilization ratio	100%	31%	96%	33%	7%	100%

Figure 10. DoFs of SURIII.

Three DoFs which are surge, heave and yaw will be researched as the main target. In surge motion, three thrusters can work simultaneously to achieve a high-speed mode and the remaining thruster can be used to brake or veer, as shown in Figure 11a,b. In addition, two opposite thrusters work together to achieve a low-speed mode, the other two thrusters can be used to brake and veer respectively, as shown in Figure 11c. In yaw motion, a gyroscope will be employed to measure the rotation angle. If all thrusters work at the same time, the robot can be realized a high-speed rotating mode which is shown in Figure 11d, this style is suitable for fast turning. Otherwise working of two opposite thrusters will realize a low-speed rotating mode. Due to the low speed, it is easier to accurately control the rotation. In heave motion, there are two kinds of motions: up and down, corresponding to Figure 11e,f.
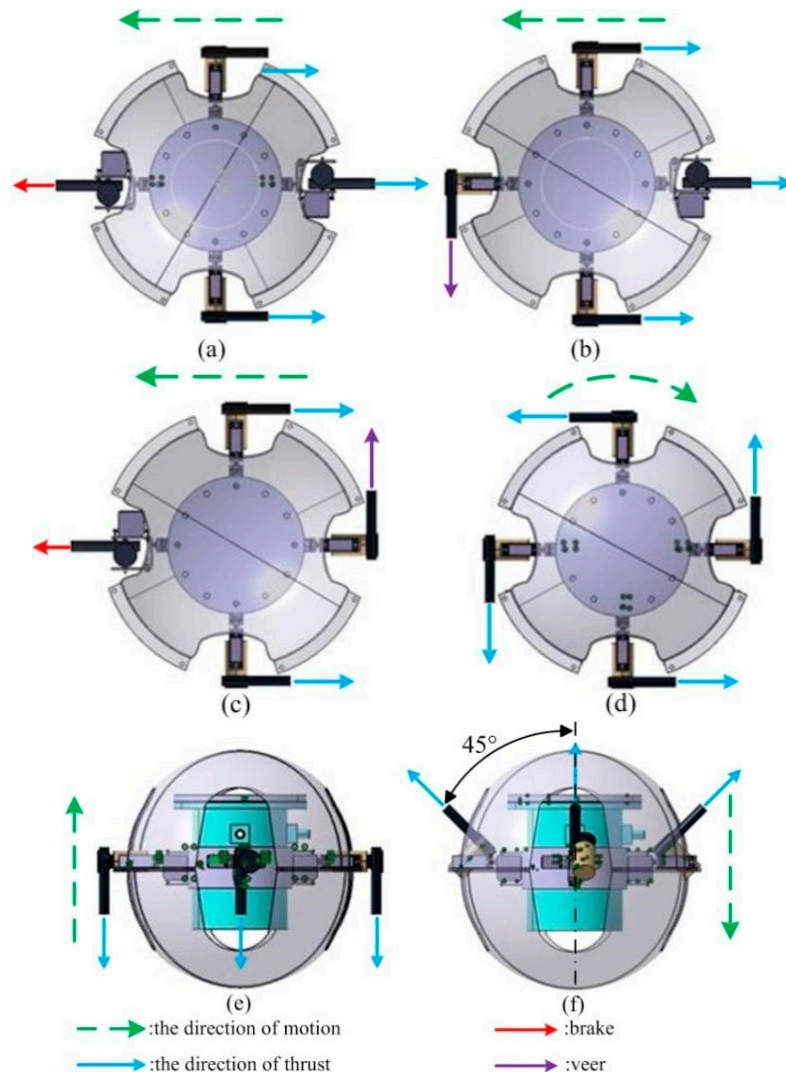

Figure 11. Motion state of SURIII.

3. Hydrodynamic Analysis

The underwater environment is complicated to the AUV. The hydrodynamic analysis of the SURIII described in this section is for getting theoretical basis which will provide initial conditions of the simulation. Before the specific analysis, some assumptions will be given firstly as follows.

1   SURIII is a spherical robot;
2   The flow field is water;
3   The temperature of flow field is 20 °C.

3.1. Dynamic Model of SURIII

Generally, the 6-DoF dynamic equation of underwater robot can be given as [21,23,24],

$$M\dot{v} + C(v)v + D(v)v + G = \tau + \tau_{wind} + \tau_{wave} \tag{1}$$

where $M \in \mathrm{R}^{6 \times 6}$ is the sum of system mass matrix and added mass matrix, $\dot{v}$ is the vector of generalized accelerations, $C(v) \in \mathrm{R}^6$ is the Coriolis and centripetal matrix. $D(v) \in \mathrm{R}^6$ is the damping matrix, $G \in \mathrm{R}^6$ is vector of restoring forces and moments, $\tau \in \mathrm{R}^6$ is the vector of generalized forces which input by control system and include the propulsive force and moment, τ_{wind} and τ_{wave} are vectors of forces generated by wind and wave. But effects of wind and wave usually occur in complicated marine environment, for our robot, these two factors can be neglectful. Hence, the dynamic equation can be simplified to Equation (2),

$$M\dot{v} + C(v)v + D(v)v + G = \tau \tag{2}$$

SURIII is a spherical robot and its structure is symmetrical, thus, M can be further simplified as follows,

$$M = \begin{bmatrix} mI_{3\times3} & 0_{3\times3} \\ 0_{3\times3} & I_{zz} \end{bmatrix} \tag{3}$$

where m is the sum of rigid body mass and added mass, I_{zz} is the resultant of inertia tensor. Also, M can be described as follows,

$$M = M_{RB} + M_A \tag{4}$$

where M_{RB} is the mass of the robot, M_A is the added mass. Moreover, $C(v)$ is the sum of rigid body and hydrodynamic Coriolis matrix, so it can be expressed as,

$$C(v) = C_{RB}(v) + C_A(v) \tag{5}$$

The Coriolis force is generated by the rotation of the robot. The rotation speed of the SURIII is minute, so $C(v)$ can be ignored in the hydrodynamic analysis. $D(v)$ is an important parameter for the hydrodynamic analysis of the underwater robot. It contains the linear damping term D_1 and nonlinear damping term $D_q(v)$ and $D(v)$ is give as,

$$D(v) = D_1 + D_q(v) \tag{6}$$

G is the restoring force which contains gravity and buoyancy. It has been mentioned before that the SURIII has four DoFs: surge, sway, heave and yaw. In this research, the SURIII is considered as the suspended status underwater, the gravity is equals to the buoyancy. So, the influence of gravity and buoyancy can be ignored. Finally, the Equation (1) can be simplified as follows,

$$(M_{RB} + M_A)\dot{v} + (D_1 + D_q(v))v = \tau \tag{7}$$

3.2. Related Parameters

M_{RB} is received by weighing the robot in air. The SURIII is 6.9 kg, so the 3D model is:

$$M_{RB} = \begin{bmatrix} m & 0 & 0 \\ 0 & m & 0 \\ 0 & 0 & I_{zz} \end{bmatrix} = \begin{bmatrix} 6.9 & 0 & 0 \\ 0 & 6.9 & 0 \\ 0 & 0 & 0.1615 \end{bmatrix} \tag{8}$$

M_A is the mass of a fluid sphere, so its 3D model is:

$$M_A = \begin{bmatrix} 16.75 & 0 & 0 \\ 0 & 16.75 & 0 \\ 0 & 0 & 0.3864 \end{bmatrix} \qquad (9)$$

The coefficients of linear damping force can be expressed as:

$$D_1 v = C_1 \times diag\{u, v, w, r\} \qquad (10)$$

The initial conditions stipulate that the temperature of water is 20 °C. At this temperature, the linear viscous coefficient is $C_1 = 1 \times 10^{-4}$. The *diag* $\{u,v,w,r\}$ is the velocity matrix of the SURIII, where u is the velocity of the surge motion, v is the velocity of the sway motion, w is the velocity of heave motion, r is the rotation velocity of the yaw motion. These two parameters are both very small, so $D_1 v$ can be ignored. The Equation (7) may be expressed as:

$$(M_{RB} + M_A)\dot{v} + D_q(v)v = \tau \qquad (11)$$

where $D_q(v)v$ equals to the resistance of the robot underwater,

$$D_q(v)v = F_d = \frac{1}{2}C_d \rho V^2 A \qquad (12)$$

where F_d is the drag of water, C_d is the drag coefficient, ρ is the density of the fluid, V is the relative speed between SURIII and fluid in different motions, A is the effective cross-sectional area of SURIII.

For surge motion, the SURIII could be approximately as a sphere. In this case, C_d only associated with the Reynolds number [25] and its formula is:

$$R_e = \frac{uD}{v} \qquad (13)$$

where R_e is the Reynolds number, u is the velocity of the surge motion, D is the diameter of the robot, v is the kinematic viscosity of the water and $v = 1 \times 10^{-6}$ Pa·s at the temperature of 20 °C. The experimental maximum velocity of surge motion is 0.15 m/s [11], the diameter of the robot is 0.4 m, so the R_e equals to 6×10^4 and this value is more than 10^4 and less than 3×10^5. The drag coefficient in surge motion can be selected from Table 2 [26,27]. If R_e equals to 6×10^4, C_d is 0.4.

Table 2. Relationship between Reynolds number and drag coefficient for the sphere.

R_e	$R_e < 10^4$	$10^4 < R_e < 3 \times 10^5$	$3 \times 10^5 < R_e < 10^6$
C_d	$24/R_e + 6.48 \times R_e^{-0.573} + 0.36$	0.4	0.4
C_d	$30/R_e + 0.46$	0.46	0.46
C_d	$24/R_e + (1 + 0.0654\,R_e^{2/3})^{2/3}$	0.4	0.40
C_d	$(0.325 + (0.124 + 24/R_e^{1/2}))$	-	-
C_d	$(0.63 + 4.8 \times R_e^{-0.5})^2$	0.4	-

In heave motion, the robot cannot be regarded as a sphere. On the one hand, for the case shown in Figure 11a, there are four gaps for the water-jet thrusters and the fluid will flow across these gaps, so that the robot cannot be classified as a closed sphere in this motion. On the other hand, for the case shown in Figure 9, the edge of hull cannot be ignored for heave motion, so that the two hemispheres

cannot form a smooth sphere and the diameter of the hull is transformed to 46 cm. According to the Equation (12), the C_d can be expressed as:

$$C_d = \frac{2F_d}{\rho V^2 A} \tag{14}$$

In Equation (14), the maximum experimental velocity of heave motion is 0.083 m/s [11]. The maximum cross-sectional area can be obtained by the projection of 3D model in the vertical direction, so *A* is 0.1661 m^2. The drag of water cannot be calculated in this case, thus the CFD simulation is conducted to get the estimation of it.

4. CFD Simulation

In this research, all the simulations were calculated by CFX which is associated with ANSYS WORKBENCH. The basic steps of CFD analysis is listed as followings,

    A. Analysis of physical problems and pre-processor of the hydrodynamic model;
    B. Solver execution;
    C. Results of the post-processing.

4.1. Pre-Processor of the CFD Simulation

The pre-processor of the hydrodynamic model includes many contents. Firstly, in the design process, some details need to be added in the 3D model of the robot to make it closer to the prototype. However, it is necessary to simplify the 3D model for CFD simulation, so that it can get effective results and reduce the computational time. The simplified parts are as follows:

(1)   The thruster has some complicated surfaces and their area are very small, so these surfaces are pre-processed as regular surfaces;
(2)   Some irregular solids have been changed to cylinder or cuboid shape;
(3)   Some parts such as screws and nuts have been omitted. And the simulation models are shown in Figure 12.

Secondly, for CFD simulation, another important model is the flow field. The flow field will affect the hydrodynamic characteristic of the robot, so it needs to be established base on the robot. The boundary of the flow field should be large enough, so it will avoid influence the domain around the robot. A cylinder with the diameter of 2 m and the height of 4 m is chosen as the flow field and the robot is put in the center of it. However, in hydrodynamic analysis, it generally needs a computational domain. The computational domain can be obtained by using Boolean operation between 3D model and flow field. The complete hydrodynamic model is shown in Figure 13.

Thirdly, the boundary conditions of the hydrodynamic model are set in the pre-processor. In this research, boundaries make up of inlet, outlet and wall which are shown in Figure 14. For different motions, it only needs to adjust the relationship between the robot and the direction of the inlet. The inlet velocity of the forward motion is 0.15 m/s and the inlet velocity of up and down motion is 0.083 m/s. The flow field is the turbulence handled by the k − ε model. The mesh is also the crucial step of hydrodynamic analysis. It is generated by using the curvature method. This method can refine the element size of the edge and curve surface. In this hydrodynamic model, the robot is considered as a suspended status. At the present step, the gravity and buoyancy are both ignored. The environment condition is set as the isothermal temperature of 20 °C.
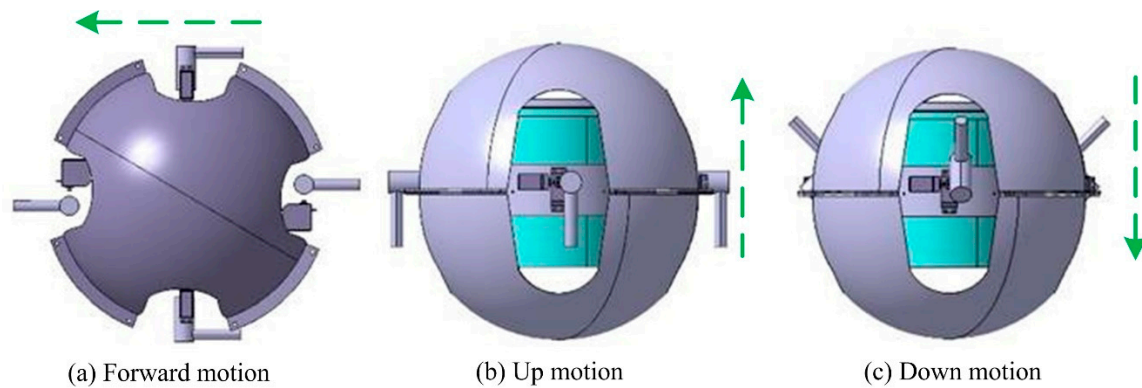
(a) Forward motion　　　　　　(b) Up motion　　　　　　(c) Down motion

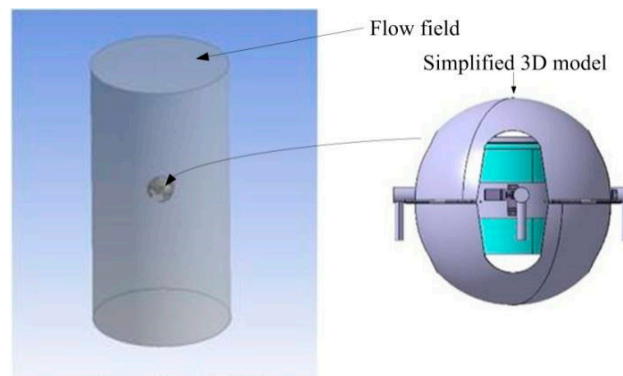**Figure 12.** Simulation model of SURIII.
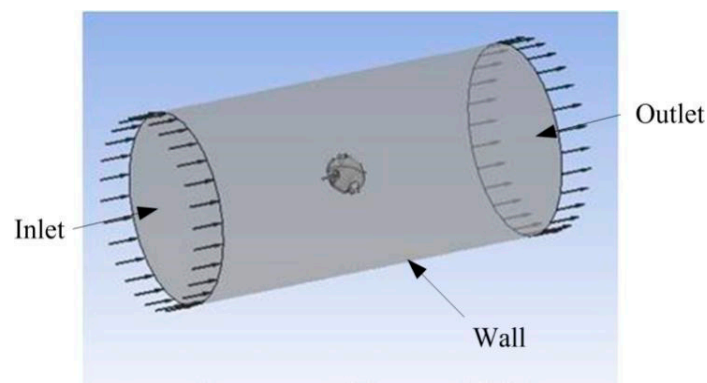

Figure 13. Flow field of SURIII.

Figure 14. Fluid boundary setting.

Finally, the convergence criterion is set as 1×10^{-4} in the solver control. Three hydrodynamic models (up, down and forward) are calculated for the CFD simulation.

4.2. Results in the Post-Processing

After solver execution, some results can be extracted from the post-processor of ANSYS CFX. In heave motion, there are two kinds of motions: up and down. Figure 15 shows the simulation results of the down motion. Figure 15a is the pressure contour for the down motion, the maximum pressure occurs in the bottom of the robot and near the edge of the robot. This confirms that the influence of

the edge in heave motion cannot be ignored. Figure 15b,c display the velocity vector and velocity streamline, respectively. As these two figures shown, the velocity of the down motion also affected by the edge of the robot. Therefore, the influence of the edge needs to be considered when calculating the drag coefficient. As well, the simulation results of up motion are shown in Figure 16. Figure 16a shows the maximum pressure occurs in the top and the edge of the robot. Figure 16b,c are the velocity vector and streamline in the up motion, respectively. As with the down motion, the up motion is also affected by the edge of the robot. For both up and down motions, the water will flow through these gaps and this may have influence on the robot in the simulation. Comparing the simulation results of these two motions, the robot has larger resistance force when it sinks. The resistance of the down motion in the simulation is 0.334 N. The maximum relative velocity in the post-processor is 0.1021 m/s and the maximum cross-sectional area is 0.1661 m^2. According to the Equation (14) and the drag coefficient can be calculated as 0.386. This drag coefficient has a 3.5% error compared to drag coefficient determined by Reynolds number for the sphere. It indicates that edges and gaps in the heave motion effect little.
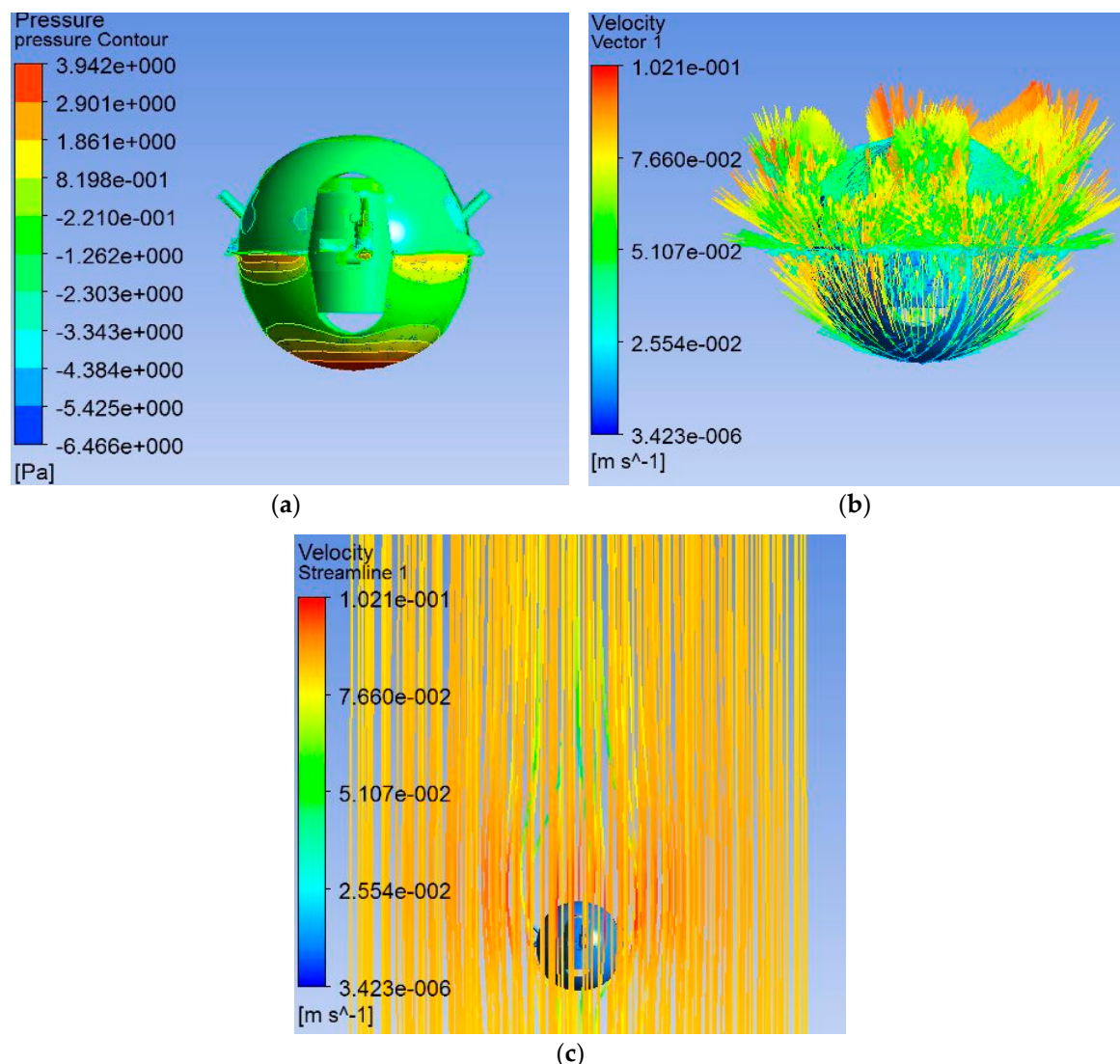

(a)

(b)

(c)

Figure 15. Down motion in heave. (**a**) Pressure contour; (**b**) Velocity vector; (**c**) Velocity streamline.
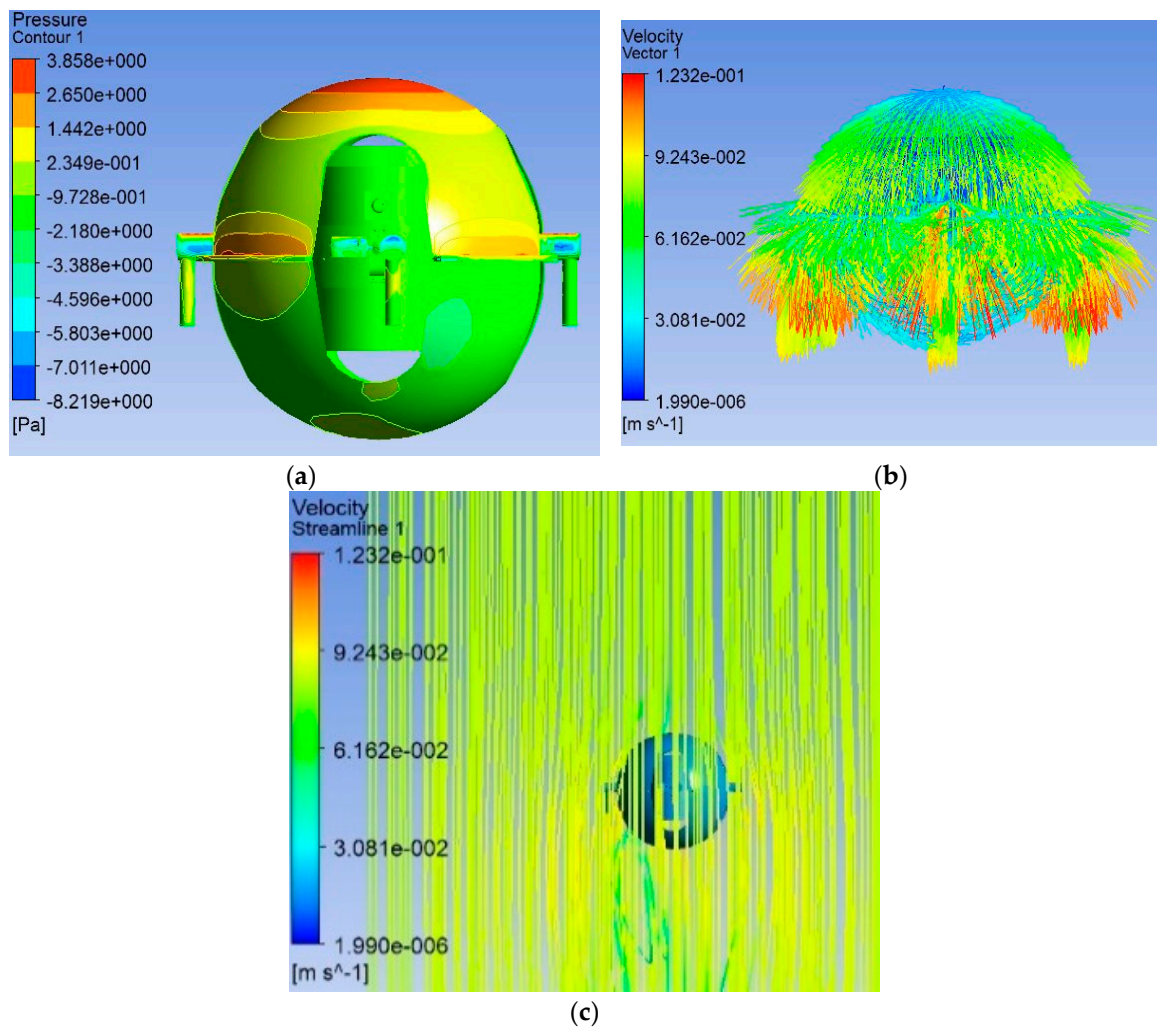
Figure 16. Up motion in heave. (**a**) Pressure contour; (**b**) Velocity vector; (**c**) Velocity streamline.

Figure 17 shows the surge motion for the SURIII, the high-speed mode is analyzed in this research, both the gaps and the edge of the robot cannot be affected to this motion. Figure 17a shows the pressure contour and the maximum pressure occurs near the edge of the robot. Figure 17b,c are the velocity vector and streamline of the high-speed surge motion and the edge can be ignored because of its small impact for the velocity vector. The resistance of the forward motion is also extracted from the post-processor to verify the drag coefficient, the force acting on the robot is 0.988 N in the flow direction, the maximum relative velocity in the post-processor is 0.1998 m/s and the maximum cross-sectional area is 0.1256 m^2. The drag coefficient can be calculated by Equation (14) and is equals to 0.394, it has a 1.5% error compared to the drag coefficient determined by Reynolds number which indicates the robot can be similarly considered as a sphere in surge motion.
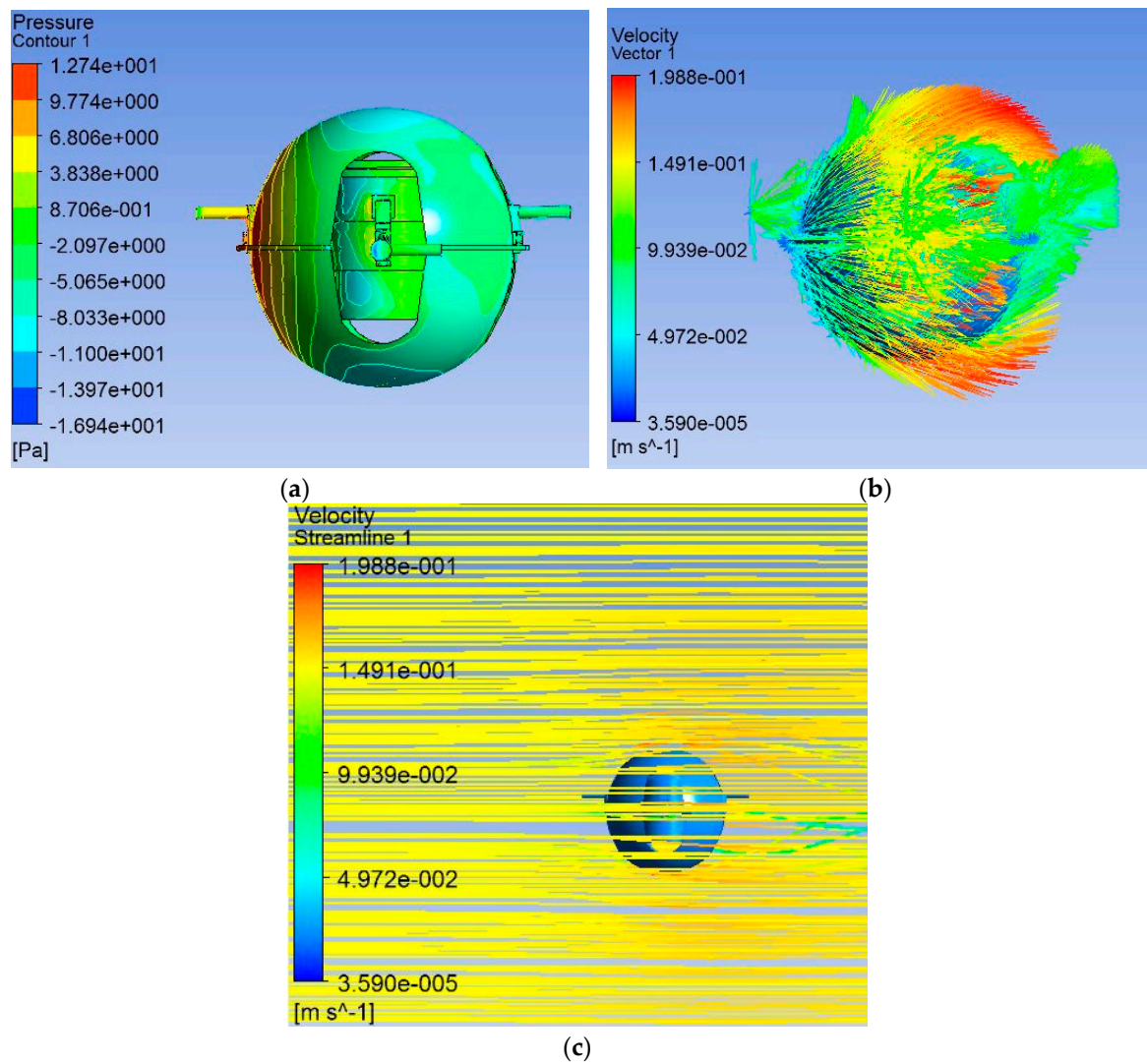
Figure 17. Forward motion in surge. (**a**) Pressure contour; (**b**) Velocity vector; (**c**) Velocity streamline.

5. Experiments and Results

For evaluating the performance of the novel propulsion system, some experiments are conducted in this section. An inflatable swimming pool is prepared with the water at the depth of 25 cm. A load cell with 6-DoF is employed to measure the propulsive force of the multi-vectored water-jet thrusters. Two power supplies are employed as the electric source and each one will give a 7.2 voltage power to two vectored water-jet thrusters. The experimental setup is shown in Figure 18. All vectored water-jet thrusters are connected with the load cell by using the aluminum alloy profile and it can be considered as rigid connection. And all the support parts of the experimental setup are also rigid bodies.

Although the SURIII has 4 DoFs, our experiments only include three different cases as the low-speed mode for the forward motion, high-speed mode for the forward motion and upward motion due to the limitation of experimental conditions. Each case will be carried out for 10 times.
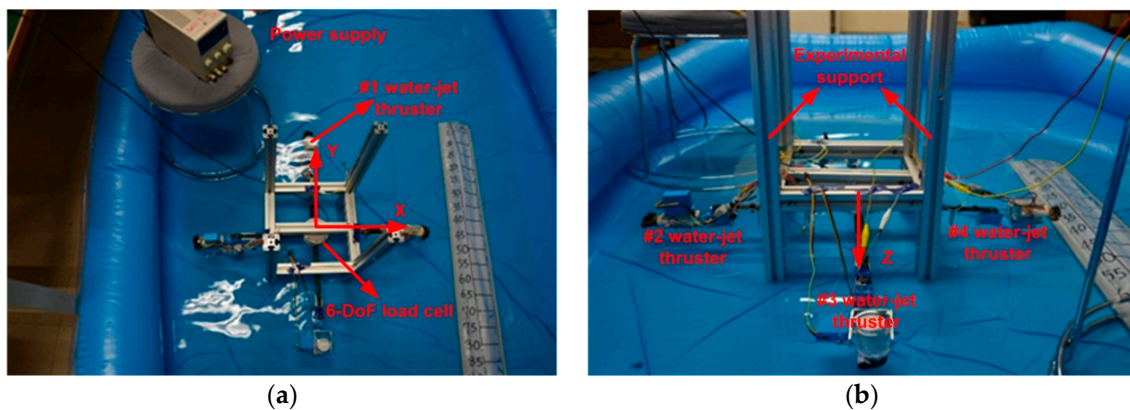
Figure 18. The experimental setup. (**a**) Top view; (**b**) Side view.

Case I: Low-speed mode for forward motion

Step 1: Choose #2 and #4 vectored water-jet thrusters to work (Figure 11c);
Step 2: Adjust the direction of propulsive forces as the Y direction;
Step 3: Set the load cell to obtain 200 values and provide the power supply at 7.2 V;
Step 4: Stop for 30 s and repeat the step 3 and 4 for 10 times.

Case II: High-speed mode for forward motion

Step 1: Choose #2, #3 and #4 vectored water-jet thrusters to work (Figure 11a);
Step 2: Adjust the direction of propulsive forces as Y direction;
Step 3: Set the load cell to obtain 200 values and provide the power supply at 7.2 V;
Step 4: Stop for 30 s and repeat the step 3 and 4 for 10 times.

Case III: Up motion

Step 1: Choose #1, #2, #3 and #4 vectored water-jet thrusters to work (Figure 11e);
Step 2: Adjust the direction of propulsive forces as Z direction;
Step 3: Set the load cell to obtain 200 values and provide the power supply at 7.2 V;
Step 4: Stop for 30 s and repeat the step 3 and 4 for 10 times.

Figure 19 displays the experimental results. The average propulsive force for each time is shown in each case. The average propulsive forces of 10 experiments for each case are 3.57 N, 5.36 N and 7.27 N, respectively. In our previous research, the SURII also has two modes for forward motion. Although an experiment which measured propulsive force of single thruster was conducted, the propulsive force of the high-speed motion and up motion can be calculated by vector synthesis. The maximum propulsive force of forward motion is $2\sqrt{3}$ N. The maximum propulsive force of up motion is 6 N [21]. It indicates that the propulsive force of the novel propulsion system in forward and up motion is better than before. In this experiment, the vectored water-jet thrusters performed in a stable manner. In either case, the changed amplitude of the propulsive force compared with the average value is within 6%.

The Equation (11) shows the relationship between mass, resistance and propulsive force. Although the SURIII is 0.6 kg heavier than SURII in air, the resistance variety is not greater than the previous research [21]. The variety of mass underwater is less than that in air and the propulsive force is improved significantly, so the speed of the SURIII will be enhanced. When the robot moves at a constant speed, the acceleration is equal to 0, then from Equation (11) the resistance can be obtained and is equals to the propulsive force. The movement process of the SURIII can be inferred, the initial stage is an acceleration process, the propulsive force will be greater than the resistance, then the speed of the robot reaches a constant, the propulsive force will be the same as the resistance, finally the robot reaches the target and the speed is slow down, the propulsive force will be less than the resistance.
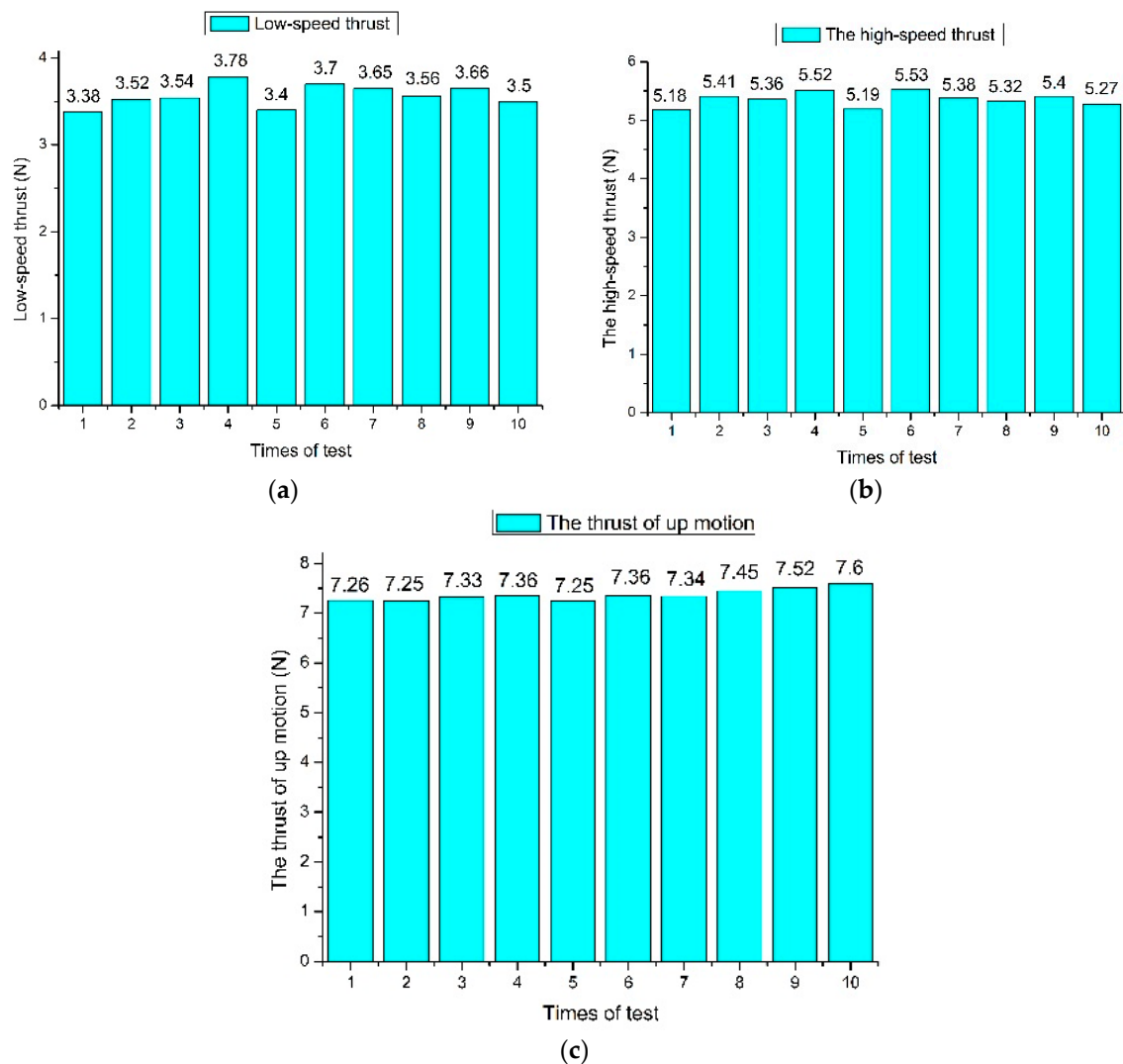
Figure 19. The average propulsive force of different experimental cases. (**a**) Case I; (**b**) Case II; (**c**) Case III.

6. Conclusions

A novel spherical underwater robot which has more stable propulsion system and better hydrodynamic performance than a previous version was developed. Firstly, a novel propulsion system was proposed to improve the dynamic performance and stability of the SURIII. Although one more water-jet thruster increases the weight of the robot from 6.3 kg to 6.9 kg, the improvement of performance for the robot more than offsets the additional weight. In the up and forward motions, the direction of the propulsive force is aligned with the direction of motion, rather than merely having a component along it. Therefore, this kind of propulsion system can provide greater propulsive force for the underwater robot. Secondly, the hydrodynamic analysis of the SURIII was presented as two different motions: surge and heave. According to the influence of edges and gaps in the SURIII, two kinds of methods were given to analyze the drag coefficient. In surge motion, the drag coefficient is 0.4 which can be selected according to the Reynolds number. Thirdly, the hydrodynamic model for CFD simulation was established. Some relevant parameters and conditions were presupposed in the pre-processing. And the pressure contours, velocity vectors and velocity streamlines were obtained from the post-processing. The maximum pressure occurred in the top, bottom and near the edge in heave motion. The maximum resistance was obtained in down motion. The drag coefficient was calculated by hydrodynamic equation and it equals to 0.386. This indicates that edges and gaps effect

little. The calculated drag coefficient in surge motion is 0.394, it has a 1.5% error compared with the chosen one, which indicates the robot can be similarly considered as a sphere. Finally, the experiment is conducted for measuring the propulsive force of multi-vectored water-jet thrusters. The experimental results indicate that the propulsive force is greater than that of the previous version. The changed amplitude of the propulsive force is within 6%.

Author Contributions: Shuxiang Guo and Shuoxin Gu co-organized the work; Shuxiang Guo and Shuoxin Gu conceived and designed the simulation and experiment work; Shuoxin Gu performed the simulation and experiment work; Shuxiang Guo contributed analysis and experiment tools; Shuoxin Gu wrote the paper; Shuxiang Guo have made substantial contributions to guide and revise the manuscript.

Conflicts of Interest: The authors declare no conflict of interest.

References

1. Galerne, E. Epaulard ROV used in NOAA polymetallic sulfide research. *Sea Technol.* **1983**, *24*, 40–42.
2. Russell, B.W.; Veerle, A.I.H.; Timothy, P.L.B.; Bramley, J.M.; Douglas, P.C.; Brian, J.B.; Henry, A.R.; Kirsty, J.M.; Jeffrey, P.; Daniel, R.P.; et al. Autonomous Underwater Vehicles (AUVs): Their past, present and future contributions to the advancement of marine geoscience. *Mar. Geol.* **2014**, *352*, 451–468.
3. Mazumdar, A.; Fittery, A.; Ubellacker, W.; Asada, H.H. A ball-shaped underwater robot for direct inspection of nuclear reactors and other water-filled infrastructure. In Proceedings of the Robotics and Automation (ICRA) 2013 IEEE International Conference, Karlsruhe, Germany, 6–10 May 2013; pp. 3415–3422.
4. Bhattacharyya, S.; Asada, H.H. Single jet impinging vertical motion analysis of an underwater robot in the vicinity of a submerged surface. In Proceedings of the 2016 IEEE Oceans Conference, Shanghai, China, 10–13 April 2016; pp. 1–8.
5. Kim, H.J.; Lee, J. Swimming Pattern Generator Based on Diving Beetles for Legged Underwater Robots. *Int. J. Mater. Mech. Manuf.* **2014**, *2*, 101–106.
6. Lin, X.; Guo, S.; Tanaka, K.; Hata, S. Underwater experiments of a water-jet-based spherical underwater robot. In Proceedings of the 2011 IEEE International Conference on Mechatronics and Automation, Beijing, China, 7–10 August 2011; pp. 738–742.
7. Lin, X.; Guo, S. Development of a spherical underwater robot equipped with multiple vectored water-jet-based thrusters. *J. Intell. Robot. Syst.* **2012**, *67*, 307–321. [CrossRef]
8. Yue, C.; Guo, S.; Li, M.; Li, Y.; Hirata, H.; Ishihara, H. Mechatronic system and experiments of a spherical underwater robot: SUR-II. *J. Intell. Robot. Syst.* **2015**, *80*, 325. [CrossRef]
9. Yue, C.; Guo, S.; Shi, L. Design and performance evaluation of a biomimetic microrobot for the father-son underwater intervention robotic system. *Microsyst. Technol.* **2016**, *22*, 831–840. [CrossRef]
10. Li, Y.; Guo, S.; Yue, C. Preliminary Concept of a Novel Spherical Underwater Robot. *Int. J. Mechatron. Autom.* **2015**, *5*, 11–21. [CrossRef]
11. Li, Y.; Guo, S.; Wang, Y. Design and Characteristics Evaluation of a Novel Spherical Underwater Robot. *Robot. Auton. Syst.* **2017**, *94*, 61–74. [CrossRef]
12. Li, Y.; Guo, S. Communication between Spherical Underwater Robots Based on the Acoustic Communication Methods. In Proceedings of the 2016 IEEE International Conference on Mechatronics and Automation, Harbin, China, 7–10 August 2016; pp. 403–408.
13. Kim, H.J.; Song, S.H. A turtle-like swimming robot using a smart soft composite (SSC) structure. *Smart Mater. Struct.* **2012**, *22*, 14007. [CrossRef]
14. Yue, C.; Guo, S.; Li, Y.; Li, M. Bio- Inspired robot launching system for a mother-son underwater manipulation task. In Proceedings of the 2014 IEEE International Conference on Mechatronics and Automation, Tianjin, China, 3–6 August 2014; pp. 174–179.
15. Watson, S.A.; Crutchley, D.J.P.; Green, P.N. The design and technical challenges of a micro-autonomous underwater vehicle AUV. In Proceedings of the 2011 IEEE/ICMA International Conference on Mechatronics and Automation, Beijing, China, 7–10 August 2011; pp. 567–572.

16. Waston, S.A.; Green, P.N. Propulsion System for Micro-Autonomous Underwater Vehicles (μAUVs). In Proceedings of the 2010 IEEE Conference on Robotics, Automation and Mechatronics, Singapore, 28–30 June 2010; pp. 435–440.

17. Fittery, A.; Mazumdar, A.; Lozano, M.; Asada, H.H. Omni-Egg: A smooth, spheroidal, appendage free underwater robot capable of 5 DOF motions. In Proceedings of the IEEE Oceans, Hampton Roads, VA, USA, 14–19 October 2012; pp. 1–5.

18. Guo, S.; Du, J.; Ye, X.; Gao, H.; Gu, Y. Realtime adjusting control algorithm for the spherical underwater robot. *Inf. Int. Interdiscip. J.* **2010**, *13*, 2021–2029.

19. Guo, S.; Du, J.; Ye, X.; Yan, R.; Gao, H. The computational design of a water-jet propulsion spherical underwater vehicle. In Proceedings of the 2011 IEEE International Conference on Mechatronics and Automation, Beijing, China, 7–10 August 2011; pp. 2375–2379.

20. Gemmell, B.J.; Costello, J.H.; Colin, S.P.; Stewart, C.J.; Dabiri, J.O.; Tfti, D.; Priya, S. Passive energy recapture in jellyfish contributes to propulsive advantage over other metazoans. *Proc. Natl. Acad. Sci. USA* **2013**, *110*, 17904–17909. [CrossRef] [PubMed]

21. Yue, C.; Guo, S.; Shi, L. Hydrodynamic Analysis of the Spherical Underwater Robot SUR-II. *Int. J. Adv. Robot. Syst.* **2013**, *10*, 1–12. [CrossRef]

22. Jiang, X.; Feng, S.; Wang, L. *Unmanned Underwater Robot*; Liaoning Science and Technology Publishing House: Shengyang, China, 2000.

23. Fossen, T.I. *Guidance and Control of Ocean Vehicles*; John Wiley & Sons Inc.: Hoboken, NJ, USA, 1994.

24. Lin, X.; Guo, S.; Tanaka, K.; Hata, S. Development and Evaluation of a Vectored Water-jet-based Spherical Underwater Vehicle. *Information* **2010**, *13*, 1985–1998.

25. Houghton, E.L.; Carpenter, P.W. *Aerodynamics for Engineering Students*, 5th ed.; Butterworth-Heinemann: Oxford, UK, 2013; pp. 8–15.

26. Ceylan, K.; Altunbas, A.; Kelbaliyez, G. A new model for estimation of drag force in the flow of Newtonian fluids around rigid or deformable particles. *Powder Technol.* **2011**, *119*, 250–256. [CrossRef]

27. Kundu, P.K.; Ira, M.C.; David, R.D. *Fluid Mechanics*, 5th ed.; Academic Press: Cambridge, MA, USA, 2012; pp. 4251–4472.